Published online 12 November 2022 *Nucleic Acids Research, 2022, Vol. 50, No. 21* **12515–12526**
https://doi.org/10.1093/nar/gkac1035

Structure of *Escherichia coli* heat shock protein Hsp15 in complex with the ribosomal 50S subunit bearing peptidyl-tRNA

Haaris A. Safdari[1], Sergo Kasvandik[2], Christine Polte[1], Zoya Ignatova[1], Tanel Tenson[2] and Daniel N. Wilson[1,*]

[1]Institute for Biochemistry and Molecular Biology, University of Hamburg, Martin-Luther-King-Pl. 6, 20146 Hamburg, Germany and [2]University of Tartu, Institute of Technology, 50411 Tartu, Estonia

Received September 02, 2022; Revised October 13, 2022; Editorial Decision October 18, 2022; Accepted November 09, 2022

ABSTRACT

In *Escherichia coli*, the heat shock protein 15 (Hsp15) is part of the cellular response to elevated temperature. Hsp15 interacts with peptidyl-tRNA-50S complexes that arise upon dissociation of translating 70S ribosomes, and is proposed to facilitate their rescue and recycling. A previous structure of *E. coli* Hsp15 in complex with peptidyl-tRNA-50S complex reported a binding site located at the central protuberance of the 50S subunit. By contrast, recent structures of RqcP, the Hsp15 homolog in *Bacillus subtilis*, in complex with peptidyl-tRNA-50S complexes have revealed a distinct site positioned between the anticodon-stem-loop (ASL) of the P-site tRNA and H69 of the 23S rRNA. Here we demonstrate that exposure of *E. coli* cells to heat shock leads to a decrease in 70S ribosomes and accumulation of 50S subunits, thus identifying a natural substrate for Hsp15 binding. Additionally, we have determined a cryo-EM reconstruction of the Hsp15-50S-peptidyl-tRNA complex isolated from heat shocked *E. coli* cells, revealing that Hsp15 binds to the 50S-peptidyl-tRNA complex analogously to its *B. subtilis* homolog RqcP. Collectively, our findings support a model where Hsp15 stabilizes the peptidyl-tRNA in the P-site and thereby promotes access to the A-site for putative rescue factors to release the aberrant nascent polypeptide chain.

INTRODUCTION

Stress conditions, such as heat shock, lead to the rapid production of heat shock proteins (1). In *Escherichia coli*, a total of 77 genes were found to be upregulated in response to heat shock at 50°C, including *groEL*, *groES*, *dnaK*, *dnaJ* and *hslR* (2). The heat-shock locus R (*hslR*, formerly *yrfH*) gene encodes the heat shock protein 15 (Hsp15), a 15 kDa protein that is upregulated by 43-fold upon temperature upshift (2). Unlike most heat shock proteins that generally function as molecular chaperones or proteases to maintain the native state of proteins, Hsp15 contains an RNA-binding domain, leading to the suggestion that it interacts with an RNA substrate (3,4). Consistently, the crystal structure of *E. coli* Hsp15 revealed a single compact globular RNA binding domain, which is found in other RNA-binding proteins such as ribosomal protein S4 and threonyl-tRNA synthetase. In addition, *E. coli* Hsp15 contains a long C-terminal α-helix (5), which is absent in Hsp15 homologs from some species, such as *Bacillus subtilis* (Figure 1) (3,4). *E. coli* Hsp15 was shown *in vivo* to associate with ribosomal 50S subunits, but not 70S ribosomes, and that this association was dependent on the presence of the nascent polypeptide chain (6). This led to the suggestion that Hsp15 binds to 50S particles containing peptidyl-tRNA that result from erroneous dissociation of elongating 70S ribosomes (6). Interestingly, increased association of Hsp15 with the 50S subunit was observed when the cells were heat shocked, however, it was not directly demonstrated whether these conditions lead to 70S dissociation (6). A cryo-electron microscopy (cryo-EM) structure of *E. coli* Hsp15 in complex with a 50S subunit containing a peptidyl-tRNA was reported at 10 Å resolution, revealing that Hsp15 is located below the central protuberance where it interacts with H84 of the 23S rRNA and the elbow region of the P-site tRNA (7). In this latter study, Hsp15 was proposed to stabilize the peptidyl-tRNA in the P-site to allow access of putative rescue factors to the A-site in order to release the aberrant nascent polypeptide chain (7).

Recently, structures of the *B. subtilis* Hsp15 homologue RqcP (formerly YabO) have been determined in complex with the ribosomal 50S subunit bearing a peptidyl-tRNA (8–10). Surprisingly, the binding position of *B. subtilis* RqcP was different than that observed for *E. coli* Hsp15. In the *B. subtilis* structures, RqcP was observed to interact with H69 of the 23S rRNA as well as with the anticodon-stem loop of the P-site tRNA (8–10). RqcP works together with RqcH

*To whom correspondence should be addressed. Tel: +49 40 42838 2841; Email: daniel.wilson@chemie.uni-hamburg.de

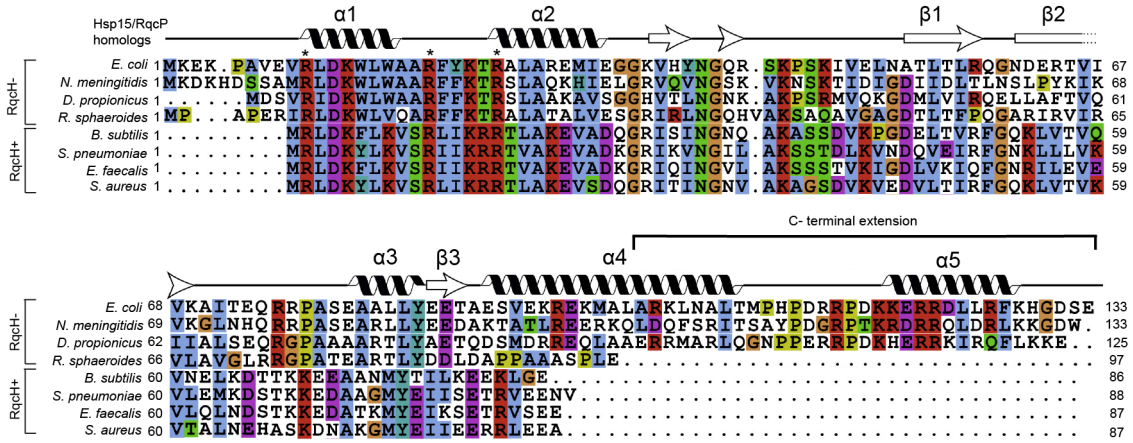

Figure 1. Sequence alignment of Hsp15/RqcP homologs across diverse bacteria. Sequence alignment for RqcH lacking bacteria such as *Escherichia coli*, *Niesseria meningitidis*, *Desulfobulbus propionicus* and *Rhodobacter sphaeroides*, as well as RqcH containing bacteria, such as *Bacillus subtilis*, *Streptococcus pneumoniae*, *Enterococcus faecalis*, *Staphylococcus aureus*. The secondary structure for *E. coli* Hsp15 is shown above the sequences and the C-terminal extension is indicated. Modified from reference (8).

as part of a ribosome-associated quality (RQC) control system to add polyalanine tails to the aberrant polypeptide chains on the 50S subunit and target them for degradation (11,12). RqcH is absent in *E. coli*, raising the question as to whether Hsp15 fulfils a distinct function in *E. coli*, which may explain the different binding site observed on the 50S subunit (7). We note however that in human mitochondria, the S4-domain containing RNA binding protein MTRES1 (formerly C6orf203) was bound in an analogous position as RqcP, where it also was observed to interact with H69 and P-site tRNA, as well as with a specialized mitochondrial rescue factor mtRF-R (13).

Here, we demonstrate that exposure of *E. coli* cells to heat shock leads to a reduction in 70S ribosomes and accumulation of 50S subunits. Using FLAG-tagged Hsp15 and immunoprecipitation with anti-FLAG antibodies, we have isolated Hsp15-50S-peptidyl-tRNA complexes from heat-shocked *E. coli* cells. Cryo-EM reconstruction of the Hsp15-50S-peptidyl-tRNA complex at 3.0 Å resolution reveals that Hsp15 is bound in an analogous position to that observed previously for RqcP in *B. subtilis* (8–10) and MTRES1 in human mitochondria (13), and unlike that observed previously within low resolution reconstructions of *E. coli* Hsp15-50S-peptidyl-tRNA complexes (7). Nevertheless, our results support a model where Hsp15 stabilizes the peptidyl-tRNA within the P-site, allowing access to the A-site for putative rescue factors to release the incomplete nascent polypeptide chain.

MATERIALS AND METHODS

Construct generation

Cloning was performed by Gibson assembly as described (14). The *hslR* gene was amplified with primers that incorporate FLAG tags using genomic DNA from the *E. coli* K12 BW25113 wildtype strain as a template, and the resulting PCR product was then cloned into pBAD24 vector. Genomic DNA was extracted from *E. coli* BW25113 cells using Wizard genomic DNA purification kit (Promega). Two separate recombinant plasmids were generated, one with N-terminal FLAG tag and other with C-terminal FLAG tag. For the N-terminal construct, a 5xGly-Ser (5x GS) linker was incorporated between the FLAG tag and Hsp15 sequence to generate a FLAG-5xGS-Hsp15 construct. The N-terminal FLAG-Hsp15 for the primer had the sequence 5′-G**GACTACAAAGACGATGACGACA AG***GGTAGTGGTAGTGGTAGTGGTAGTGGTAGT*AT GAAAGAGAAACCTGCTGTT-3′ (where bold bases represent the FLAG tag and italicized bases represent 5x GS linker) and the Hsp15rev primer had the sequence 5′-GATCCCCGGGTAC**TTATTCACTGTCGCCGTGTTT**-3′ where the bold sequence represents the annealing site at the 3′-end of the *hslR* gene. For vector amplification, the empty pBAD24 plasmid was used as a template with following set of primers: pBADfor with sequence 5′-CGGCGACAGTGAATAA**GTACCCGGGGATCC TCTAG**-3′ (where bold represents the annealing site within the pBAD24 vector) and pBADrev primer with the sequence 5′-T*ACTACCACTACCACTACCACTA CCACTACC***CTTGTCGTCATCGTCTTTGTAGTC**CA TGGTGAATTCCTCCTGCT-3′ (where bold represents the reverse complement of the FLAG tag sequence and italicized bases represent the reverse complement of the 5xGS linker sequence). A similar approach was used to generate the C-terminal FLAG-tagged Hsp15 in pBAD24 plasmid, yielding the Hsp15-5XGS-FLAG construct. The C-terminal Hsp15-FLAGfor had the sequence 5′-AGGAATTCACCATG**AAAGAGAAACCTGCTGTTGA G**-3′ where bold represents the annealing site for *hslR* gene and Hsp15-FLAGrev primers had the sequence 5′-CTTA**CTTGTCGTCATCGTCTTTGTAGTC***ACTA CCACTACCACTACCACTACCACTACC*TTCACTGT CGCCGTGTTTAAA-3′ (where bold represent the reverse complement of FLAG tag while italicized bases represent the reverse complement of 5X GS linker sequence). For vector amplification, pBADfor primer with following sequence was used: 5′-A*GGTAGTGGTAGTGGTAGT GGTAGTGGTAGT***GACTACAAAGACGATGACGACA AG**TAAGTACCCGGGGATCCTCTAG-3′ where italicized bases represent 5X GS linker sequence while bases

in bold encode the FLAG tag sequence) and for pBADrev primer sequence 5′- AGCAGGTTTCTCTTT**CATGGT GAATTCCTCCTGCT**-3′ where bold represent bases which anneal with pBAD24 vector backbone was used. The PCR products of vector and insert PCR reactions were assembled into isothermal reaction at 50°C for 1 h with Gibson assembly master mix (New England Biolabs, #E2611) which has three enzymatic activities in single isothermal reaction: 5′ exonuclease, 3′ extension of DNA polymerase and finally DNA ligase activity to seal and covalently link the DNA together. The correct sequence of the constructs for the recombinant N- and C-terminal FLAG-tagged Hsp15 plasmid were confirmed by Sanger sequencing.

E. coli cultures

The N- or C-terminal FLAG-tagged pBAD-Hsp15 plasmids were transformed into *E. coli* BW25113Δ*hslR* cells. The cells were grown in LB medium overnight at 37°C with 100 ng/μl ampicillin. These overnight grown cells were diluted in 1L fresh LB medium to around optical density at 600nm (OD_{600}) of 0.1 and grown until OD_{600} reached ∼0.5 with shaking at 160 rpm and induced with different concentration of arabinose, followed by harvesting at OD_{600} ∼1.5 (late log phase). The arabinose concentration of 0.00005% (v/v) was chosen for further experiments to avoid overexpression and probable non-specific binding. For heat shock experiments, cells were grown at 30°C, induced at OD_{600} of around 0.5 and heat shock was induced at the specified temperature upon reaching OD_{600} ∼1.5 for 20 min before harvesting at room temperature (to avoid cold stress) by centrifugation for 10 mins at 4000 rpm in an SS-34 rotor (ThermoFisher Scientific).

Sucrose density gradients

For sucrose density gradient experiments, *E. coli* BW25113Δ*hslR* cells with N-terminal FLAG-tag were grown at 30°C in 1 l LB medium and induced at OD_{600} 0.5 with 0.00005% (v/v) arabinose. The cells were then heat shocked at the specified temperature upon reaching OD_{600} ∼1.5 for 20 min and then 25 ml cells were harvested by centrifugation using A-4-81 rotor (Eppendorf) at 4000 rpm for 10 min at room temperature. The cells were then resuspended in HAM buffer (25 mM HEPES–KOH pH 7.46, 100 mM KOAc, 6 mM MgOAc, 0.1% NP-40 (v/v)) without dithiothreitol (DTT), lysed by using FastPrep®-24 classic beat beater (MP Biomedicals) and centrifuged using F45-30-11 rotor (Eppendorf) at 10 000 rpm for 10 min. The supernatant was then diluted to adjust the final OD at 260 nm to around 5.0. The adjusted supernatant was then layered onto 10–40% sucrose gradients containing HAM buffer (without DTT) by centrifugation in a Beckman type 45Ti rotor at 4°C at 16 000 rpm for 18 h. The gradients were pumped-out after centrifugation while monitoring continuously the absorbance at 260 nm with a Gradient Station (model B153-002 from Biocomp Instruments). The curves were exported into excel and rescaled for preparation of figures. Another set of experiments with *E. coli* BW25113Δ*hslR* cells were performed in the same way as described above with the exception of using HAM buffer containing 15 mM MgOAc instead of 6 mM MgOAc. For assessing the effect of heat on ribosomes *in vitro*, *E. coli* 30S/50S/70S particles were incubated at 37, 44, 46 or 48°C for 20 min and were subjected to sucrose density gradient centrifugation analysis in HAM buffer containing 6 mM MgOAc.

Purification of Hsp15-peptidyl tRNA-50S complexes

For the complex purification, 1 l of *E. coli* BW25113Δ*hslR* culture transformed with N-terminal FLAG-tagged pBAD-Hsp15 plasmid was grown at 30°C, induced when OD_{600} reached ∼0.5, and grown until OD_{600} reached 1.5. The 1 l culture was then heat shocked at 48°C for 20 min. The cells were then harvested using an SS34 rotor (ThermoFisher Scientific) at 4000 rpm for 10 mins at room temperature and lysed using LM10 Microfluidizer high pressure homogenizer (Microfluidics™) in three strokes at 18 000 psi in 30 ml sterile-filtered HAM buffer. The lysates were then further clarified by centrifuging in SS-34 rotor (Thermo Scientific) at 17 000 rpm for 20 min. The supernatant was incubated in pre-washed anti-FLAG M2 Affinity Gel and kept for 1.5 h on a turning wheel at 4°C. The beads were then collected by centrifugation using A-4-81 rotor (Eppendorf) at 2200 rpm for 3 min and washed twice with 20 ml HAM buffer before being loaded onto a Mobicol 'F' column with 35 μm pore size (MoBiTec). The beads were then washed thrice with 5 ml HAM buffer without NP-40 to remove any non-specific binders. The FLAG-tagged Hsp15 complexes were then eluted by adding 40 μl HAM buffer with 0.01% NP-40 (v/v) containing 0.25 mg/ml of 3X FLAG peptide for 45 min on turning wheel at 4°C, followed by additional incubation on ice for 15 min. The eluate was collected by centrifugation using F45-30-11 rotor (Eppendorf) at 2200 rpm at 4°C to collect eluate. Some portion of this eluate was retained for SDS-PAGE analysis, while rest of it was directly applied onto cryo-EM grids.

Mass spectrometry

The gel band was cut to ∼1 mm^3 pieces and then destained in 1:1 acetonitrile (ACN):50 mM 4-(2-hydroxyethyl)-1-piperazineethanesulfonic acid (HEPES) pH 8.5 buffer with vortexing. Protein reduction and alkylation was carried out with 10 mM tris(2-carboxyethyl)phosphine hydrochloride and 40 mM chloroacetamide by incubating them at 70°C for 5 min. Overnight protein in-gel digestion was carried out with 10 ng/μl of dimethylated porcine trypsin (Sigma Aldrich) in 50 mM HEPES pH 8.5 buffer at 37°C. Peptides were extracted from the gel matrix using bath sonication for 3 min, followed by 15 min vortexing in 2 volumes of 1:2 5% formic acid (FA):ACN. The organic phase was evaporated in a vacuum-centrifuge, after which the peptides were desalted on in-house made C18 (3M) solid phase extraction tips. Purified peptides were reconstituted in 0.5% trifluoroacetic acid. Easy-nLC 1200 nano-LC system (Proxeon) was used as the liquid chromatography (LC) front-end separation system. Peptides were loaded onto an in-house packed (3 μm, 100 Å C18 particles, Dr Maisch) analytical 50 cm × 75 μm emitter-column (New Objective).

Elution was carried out at 250 nL/min with a 2–35% (60 min) A to B gradient (buffer A: 0.1% (v/v) FA; buffer B: 80% (v/v) ACN + 0.1% (v/v) FA) and electrosprayed to a quadrupole-orbitrap Q Exactive Plus (Thermo Fisher Scientific) MS/MS via a nano-electrospray source (positive mode, spray voltage of 2.5 kV). The MS was operated with a top-5 data-dependent acquisition strategy. Briefly, one 350–1400 m/z MS scan at a resolution setting of $R = 70\,000$ was followed by higher-energy collisional dissociation fragmentation (normalized collision energy of 26) of the five most intense ions (z: +2 to + 5) at $R = 17\,500$. MS and MS/MS ion target values were 3 000 000 and 50 000 ions, respectively, with both ion collection times limited to 45 ms. Dynamic exclusion was set to 30 s, peptide isotopic match to 'preferred' and exclusion of isotopes was on. MS raw files were processed with the MaxQuant software package (version 2.0.3.0) (15). Methionine oxidation, protein N-terminal acetylation were set as potential variable modifications, while cysteine carbamidomethylation was defined as a fixed modification. Identification was performed against the UniProt (www.uniprot.org) *Escherichia coli* reference proteome database using the tryptic digestion rule. Only protein identifications with at least two peptides ≥7 amino acids long (with up to two missed cleavages) were accepted. Intensity-based absolute quantification (iBAQ) feature of MaxQuant was enabled (16). This normalizes protein intensities by the number of theoretically observable peptides and enables rough intra-sample estimation of protein abundance. Peptide-spectrum match, peptide and protein false discovery rate was kept <1% using a target-decoy approach. All other parameters were default.

tRNA microarrays

tRNA microarrays were performed similarly to as previously described (17). The total tRNA bound to the Hsp15-50S-peptidyl-tRNA complexes was compared on the same arrays to the total *E. coli* tRNA. A detailed protocol including data analysis is published on protocols.io (dx.doi.org/10.17504/protocols.io.hfcb3iw). To deacylate the tRNA isolated from the lysate and immunoprecipitated complexes, the samples were incubated with 125 mM Tris–HCl, pH = 9.0, 0.1 M EDTA, 0.5% (w/v) SDS at room temperature for 45 min, thereafter neutralised with an equal volume of 1 M NaOAc, pH 5.5. RNA was extracted with 5:1 acidic phenol:chloroform, precipitated with ethanol, and resuspended in ddH_2O. Using the unique invariant single stranded 3′-NCCA-ends of intact tRNAs a Cy3-labeled RNA/DNA and Atto647-labeled RNA/DNA oligonucleotides were ligated to the tRNA extracted from the Hsp15-50S-peptidyl-tRNA samples and total *E. coli* tRNA, respectively. Labeled tRNA was again purified by phenol:chloroform extraction and ligation efficiency verified on denaturing 10% SDS-PAGE. Labeled tRNA samples were loaded on a microarray containing 24 replicates of full-length tDNA probes recognizing 40 *E. coli* tRNA isoacceptors and hybridized for 16 h at 60°C. Fluorescence signals of microarrays were recorded with a GenePix 4200A scanner (Molecular Devices) and statistically analyzed as described (dx.doi.org/10.17504/protocols.io.hfcb3iw).

Cryo-EM grid preparation and data acquisition

Quantifoil holey carbon grids (Cu R3/3) with additional 3 nm continuous carbon layer (Product: C3-C18NCu30-01) was glow discharged with GloQube® Plus Glow Discharge system for 60 s at 25 mA with negative charge. Briefly, 3.5 μl of the purified sample (8 OD_{260}/ml) was applied to glow discharged grids on Vitrobot Mark IV (Thermo Fisher) with humidity 100%, blot force 0, blot time 3 s followed by rapid plunging into an ethane:propane mixture, followed by transfer and storage in liquid nitrogen. Data collection was performed using a Titan Krios (Thermo Fisher/FEI) equipped with K3 direct electron detector at super resolution mode with a nominal magnification of 105 000 × yielding a pixel size of 0.418 and defocus range of –0.5 to –1.5 μm. Total 40 e/A^2 was fractionated into 40 frames in the dose fractionation mode.

Cryo-EM Data processing

RELION 4.0 (18,19) was used for all image processing unless otherwise stated. Beam induced motion correction was performed by MotionCor2 (20) wrapper in Relion 4.0 using 5 × 5 patches and unbinning of 2 times to retain final pixel size of 0.836 at particle level. CTF estimation was done by CTTFFIND (21). Particles were picked using crYOLO (22) using pretrained general model with $t = 0.15$. A total of 955 690 particles were picked which were then extracted with 4× binning (pixel size 3.344), and used as an input in 2D classification to remove junk or non-ribosomal particles. The best 2D class averages with ribosome-like features were selected manually in subset selection job yielding 389 798 particles. These were then re-extracted with 2× binning to keep a pixel size of 1.672. A 60 Å low pass filtered *E. coli* 50S subunit map was used for consensus refinement which was then used as input for 3D classification without alignment with four classes and $T = 4$. The class with Hsp15-P-tRNA-50S complex (which comprised 64% particles) was selected and unbinned at 1× (at 0.836 pixel size) for achieving high resolution before running another round of 3D refinement to reach resolution of 3.1 Å. CTFRefine was further used to correct for various microscope parameters like anisotropic magnification, beam tilt and per-particle defocus to reach a final resolution of 3.0 Å. The final map obtained by final Refine3D after CTF refinement was sharpened by using LocScale2 (23) without using atomic model as input. Local resolution estimation was done by wrapper in Relion with soft spherical mask generated in Relion mask creation job type.

Model building

The atomic model for *E. coli* 50S subunit was based on high resolution cryo-EM structure of bacterial ribosome (PDB ID: 7K00) (24). Water and other ions were removed before rigid body fitting into the cryo-EM map using ChimeraX (25,26). The local real space refinement was done in coot (27) and P-site $tRNA^{fMet}$ (PDB ID: 7K00) (24) was refined in Coot to fit the P-site tRNA density in our map. For the P-site tRNA, nucleotides at position 33–36 were not included in the model since they could not be resolved in the cryo-EM map. For *E. coli* Hsp15, the high-resolution

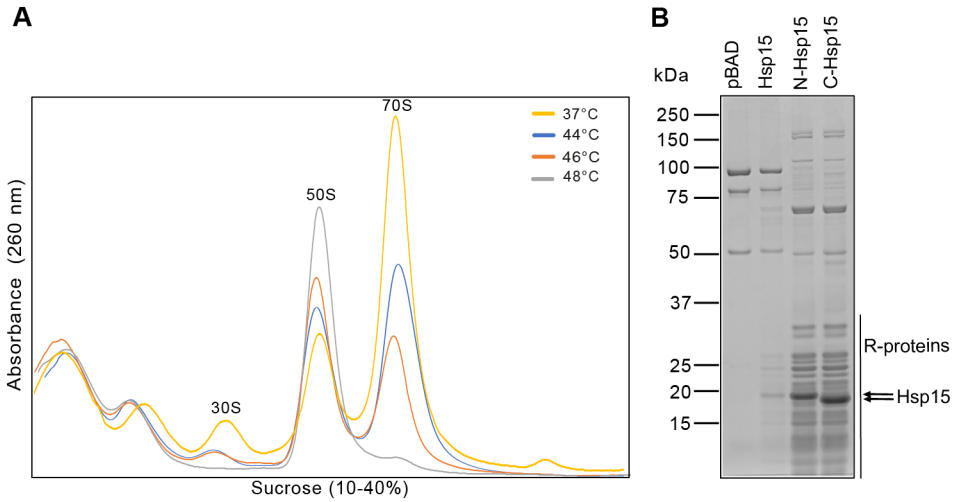

Figure 2. Characterization and immunoprecipitation of *E. coli* Hsp15-FLAG under heat shock. (**A**) Sucrose gradient density profiles of *E. coli* cell lysates expressing Hsp15 at 37°C (gold), or after heat shock at temperatures of 44°C (blue), 46°C (orange) or 48°C (grey). The position of 30S, 50S and 70S ribosomes are indicated. (**B**) SDS-PAGE analysis of FLAG-immunoprecipitation of strains bearing vector alone (pBAD), or expressing untagged Hsp15 (Hsp15), or N- (N-Hsp15) or C-terminally FLAG tagged Hsp15 (C-Hsp15). The positions of ribosomal proteins and Hsp15 proteins are indicated.

X-ray crystal structure of *E. coli* Hsp15 (PDB ID: 1DM9) (5) was used. Only residues from Pro5 to Ala106 were built corresponding to Hsp15 density. The model was manually inspected in Coot and local data fit parameters like rotamers and Ramachandran outlier were fixed in Coot and phenix.real_space_refine (28) was used for real space refinement and interactive validation and fixing the model. This was done iteratively until phenix.validation_cryoem gave acceptable model related metric and model was validated separately by Molprobity (29) (see Supplementary Table S1).

RESULTS AND DISCUSSION

Generation of *E. coli* Hsp15-ribosome complex for structural analysis

Previous studies have demonstrated that Hsp15 has higher affinity for 50S subunits bearing peptidyl-tRNA compared to vacant 50S subunits (6,7). However, in these studies the 50S-peptidyl-tRNA complexes were generated *in vitro* by reducing magnesium and increasing salt concentrations to induce dissociation of translating 70S ribosomes (6,7), rather than by investigating interaction with physiologically relevant 50S-peptidyl-tRNA complexes that arise *in vivo*. Since Hsp15 is upregulated in conditions of heat shock (2) and has a stronger association with 50S subunits under heat shock conditions (6), we rationalized that heat shock conditions may cause dissociation of elongating 70S ribosomes and accumulation of 50S subunits, and therefore represent a physiological substrate for Hsp15 binding. To investigate this, we expressed Hsp15 bearing an N- or C-terminal FLAG tag and employed affinity chromatography to isolate Hsp15-ribosome complexes directly from the cell, similar to that performed previously to obtain *B. subtilis* RqcH- and RqcP-ribosome complexes (8,9). Experiments were performed in the *E. coli* BW25113Δ*hslR* strain where the *hslR* gene encoding Hsp15 had been disabled (see Materials and Methods). Briefly, cells were grown at 30°C and Hsp15 expression was induced with arabinose during exponential phase (OD_{600} of 0.5) and then cells were transferred at late log phase (OD_{600} of 1.5) to higher temperatures (44, 46 and 48°C) for 20 min to induce heat shock conditions, before harvesting. Sucrose gradient centrifugation of the lysates revealed that heat shock, led to a strong reduction in 70S ribosomes and concomitant accumulation of 50S subunits (Figure 2A). Moreover, the effect was stronger with increasing temperature to the extent that the 70S peak had almost completely disappeared at 48°C. Curiously, accumulation of the 30S subunit was not observed, suggesting that it may be rapidly degraded under these conditions. One possibility to explain our observations is that the heat shock treatment causes 70S ribosome dissociation and the 30S subunits are then targeted for rapid degradation. However, we also cannot exclude that the 30S subunits are directly degraded within the context of 70S ribosomes, since this would also lead to the observed reduction in 70S ribosomes and accumulation of 50S subunits. To address whether heat treatment *per se* is sufficient to dissociate *E. coli* 70S ribosomes and/or degrade 30S subunits, we incubated a mixture of *E. coli* 30S/50S/70S particles at 37, 44, 46 or 48°C for 20 min and subjected the reactions to sucrose density gradient centrifugation analysis (Supplementary Figure S1). The results suggested that the heat treatment, even at the highest temperature tested of 48°C for 20 min, does not lead to significant spontaneous 70S dissociation, nor to degradation of 30S subunits (Supplementary Figure S1). Thus, we conclude that either the 30S subunits are being directly degraded within the context of the 70S ribosome, or that an active mechanism exists in the cell to dissociate 70S ribosomes following heat shock exposure, which in turn leads to rapid degradation of the 30S but not 50S subunits. Currently, we favour the latter scenario since when we repeated the *in vivo* heat shock experiments, but resuspend the lysate in buffer containing higher magnesium (15 mM instead of 6 mM), we observed a marked stabilization of the 70S ribo-

somes (and therefore 30S subunits within 70S ribosomes), i.e. more 70S ribosomes were present than 50S subunits at 48°C (Supplementary Figure S1B, C).

Since the highest peak for 50S subunit was observed with heat shock at 48°C, this condition was used for isolation of the Hsp15-ribosome complexes. Immunoprecipitation as performed with both the N- or C-terminally FLAG-tagged Hsp15 proteins, and as negative controls, we used the *E. coli* BW25113Δ*hslR* strain bearing either an empty pBAD vector control or expressing an untagged version of Hsp15. SDS-PAGE analysis of the immunoprecipitations using both the N- and C-terminally FLAG-tagged Hsp15 yielded multiple protein bands (Figure 2B), consistent with the presence of ribosomal proteins. These bands were absent or present at a low level in the immunoprecipitations performed with the strains bearing either an empty pBAD vector control or expressing an untagged version of Hsp15, respectively (Figure 2B). Since both immunoprecipitations were successful, we arbitrarily decided to continue working with the N-terminally FLAG-tagged Hsp15 for structural analysis. Next, the presence of ribosomal proteins in the elution fractions of the N-terminally FLAG-tagged Hsp15 immunoprecipitations was also confirmed using mass spectrometry (Supplementary Dataset 1). While the mass spectrometry analysis revealed ribosomal proteins from both the 30S and 50S subunits, Hsp15 (position 8) and 50S subunits represented 15 of the top 20 hits, suggesting that Hsp15-50S subunit complexes were enriched in the immunoprecipitation. Thus, the elution sample from the immunoprecipitation with the N-terminally FLAG-tagged Hsp15 was subjected to single particle cryo-EM analysis.

Cryo-EM structure of an *in vivo* formed Hsp15-50S-peptidyl-tRNA complex

Cryo-EM analysis of the elution fraction from the N-terminally FLAG tagged-Hsp15 sample identified four subpopulations of ribosomal particles (Supplementary Figure S2A). A minor population of particles (1.5%, 5364 particles) contained rotated 70S ribosomes with hybrid A/P- and P/E-tRNAs, whereas a larger population (19.5%, 76 149 particles) contained non-rotated 70S ribosomes with additional density corresponding to the ribosome-associated inhibitor A (RaiA, also termed pY or YfiA) (Supplementary Figure S2A), which was consistent with the detection of RaiA (position 51) in our mass spectrometry data (Supplementary Dataset 1). RaiA was observed in the canonical binding site, as reported previously (30–33), and no additional density for Hsp15 was observed, therefore, this population was not analyzed further. Two populations containing 50S subunits were also observed (Supplementary Figure S2A), one major population (64%, 247 060 particles) containing P-site tRNA and an additional density that we attributed to Hsp15, and a minor population (15%, 58 156 particles) that contained vacant 50S subunits, probably arising due to dissociation of the P-site tRNA and Hsp15 during sample preparation. Thus, the major population of 50S subunits containing P-site tRNA and Hsp15 were refined further, yielding a final cryo-EM reconstruction with an average resolution of 3.0 Å (Figure 3A and Supplementary Figure S2B).

Although the cryo-EM density for the 50S subunit was well-resolved, consistent with the average resolution, the densities for the P-site tRNA and Hsp15 were less ordered (Supplementary Figure S3A–L). Local resolution calculations indicate that the acceptor arm of the P-site tRNA was relatively stable with the CCA-end well-resolved (Supplementary Figure S3A–C), probably due to its stable interaction with the P-loop at the peptidyltransferase center (PTC). By contrast, the elbow and anticodon stem of the P-site tRNA exhibited progressively increased flexibility and lower resolution as they extend away from the 50S (Supplementary Figure S3A-C). Similarly, local resolution calculations indicated flexibility for Hsp15 (Supplementary Figure S3D–F), presumably due to its major interaction with the flexible anticodon stem of the P-site tRNA. Nevertheless, the local resolution of the core of Hsp15 was around 4 Å (Supplementary Figure S3D–F), where secondary structure features are prominent, making it possible to unambiguously fit an alpha-fold homology model for Hsp15 that encompasses the entire RNA-binding domain (residues 9–71) as well as the proximal portion of the C-terminal α4-helix (residues 89–106) (Figure 3B and Supplementary Table S1). The remaining C-terminal residues 107–133 (including α5-helix) were completely disordered and could not be modelled (Figure 3B). For the P-site tRNA, the resolution was sufficient to generate a model for the acceptor and anticodon stems, however, the anticodon stem loop (nucleotides 33–36) was poorly resolved and therefore not modeled (Figure 3C). The resolution was also insufficient to discern whether a specific tRNA species was present, or whether it represented a mixture of different tRNA species. To address this, we performed tRNA microarray analysis comparing the identity and levels of tRNAs bound to the Hsp15-50S-peptidyl-tRNA complex versus the total tRNAs present in the lysate (Figure 3D). We did not observe enrichment of $tRNA^{Ala}$, as observed previously in *B. subtilis* RqcH-50S-peptidyl-tRNA complexes (8,11), nor tRNAs bearing amino acids that can promote translation pausing e.g. $tRNA^{Pro}$, (34–36). Rather we saw enrichment in one $tRNA^{Leu}$(GAG) isoacceptor decoding CUC and CUU codons (Figure 3D). While the reason for the enrichment of this specific $tRNA^{Leu}$(GAG) is unclear, we note that is enrichment is quite modest over the unspecific background signals. Thus, collectively, the overall mixture of different tRNAs present in the Hsp15-50S-peptidyl-tRNA pull-downs is consistent with the idea that the 50S-peptidyl-tRNA complexes that arise from heat shock come from the polysome or translating 70S ribosomes. If this were the case, then one would expect that the P-site tRNA contains a nascent polypeptide chain within the exit tunnel of the Hsp15-50S-P-tRNA complexes. Indeed, additional density is observed extending from the CCA-end of the P-site tRNA past the tunnel constriction towards the tunnel exit at the solvent side of the large subunit (Figure 3E). The density is poorly resolved, which would be consistent with a mixture of different nascent polypeptide chains, however, although unlikely, we cannot exclude that a defined polypeptide sequence is present in the tunnel but exhibiting high flexibility.

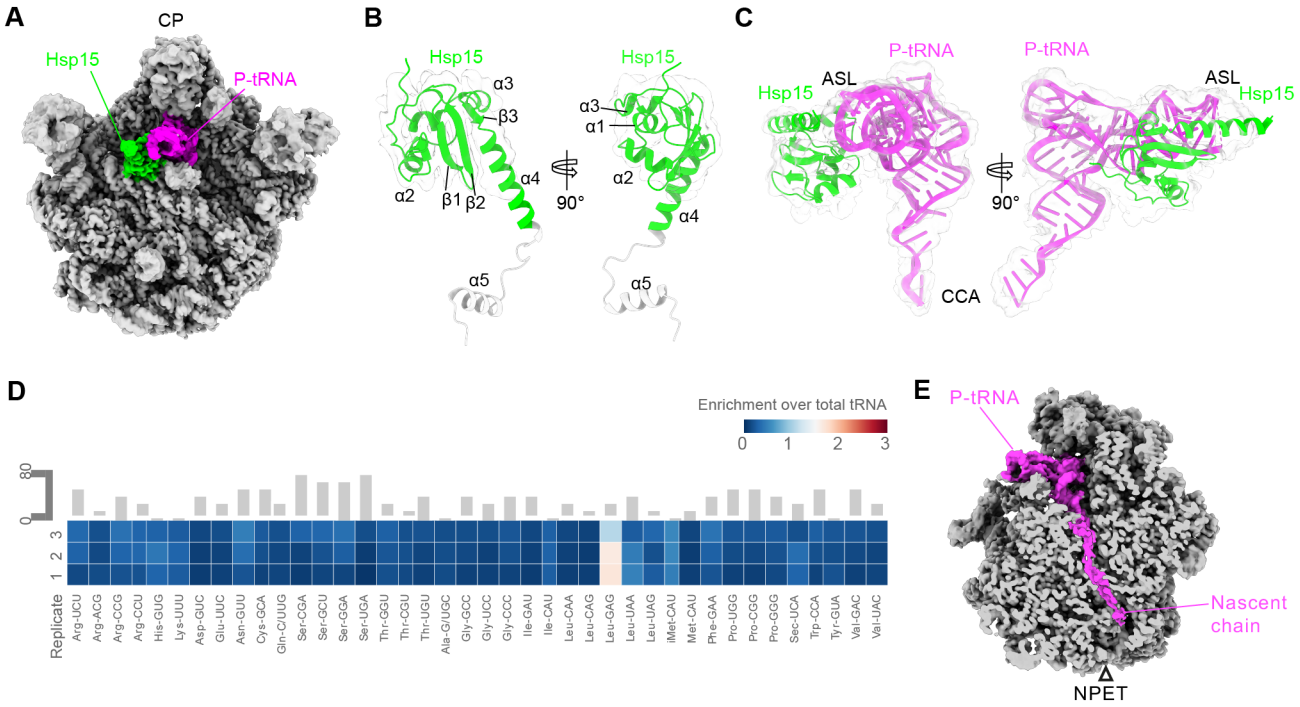

Figure 3. Cryo-EM structure of *E. coli* Hsp15-peptidyl-tRNA-50S complex. (**A**) Crown view of the non-segmented cryo-EM map of *E. coli* Hsp15-peptidyl-tRNA-50S complex with colour zoned densities for Hsp15 (lime) and P-site tRNA (magenta). The cryo-EM density for 50S subunit is grey with central protuberance (CP) indicated for orientation. (**B**) Two views of the isolated cryo-EM density (transparent grey) with fitted model for Hsp15 (lime). Note that the C-terminal residues 107–133 of Hsp15 (grey) were disordered and could not be modelled. This region includes the terminal alpha-helix a5 and is shown based on AlphaFold prediction only for illustration. (**C**) Two views of the isolated cryo-EM density (transparent grey) with fitted model for Hsp15 (lime) and P-site tRNA, with CCA-end and anticodon stem loop (ASL) labelled for orientation. (**D**) tRNA microarray analysis of the *E. coli* Hsp15-peptidyl-tRNA-50S complex. Three replicates are shown with the grey bars representing an example of covariance analysis between replicates 1 and 3. Confidence intervals between replicates 1 and 2, 2 and 3, and 1 and 3 were 97%, 94%, and 96%, respectively. Color key indicates the fold-enrichment over lysate. iMet, initiator $tRNA^{Met}$. (**E**) Transverse section of the *E. coli* Hsp15-peptidyl-tRNA-50S complex showing the continuous density for the nascent chain running through the nascent peptide exit tunnel (NPET).

E. coli Hsp15 interacts with P-site tRNA and H68-H69 of the 23S rRNA

Although the resolution does not allow for a molecular description of the interactions of Hsp15 with the P-site tRNA or ribosomal components, a more general description is possible. The Hsp15 binding site is located on the E-site side of the P-site tRNA, where it wedges between the junction of H68 and H69 of the 23S rRNA and the anticodon-stem of the P-site tRNA (Figure 4A, B). This is consistent with the surface charge distribution of Hsp15, with many positively charged residues forming two clusters, cluster 1 (C1) oriented towards the P-site tRNA and cluster 2 (C2) at the junction of H68 and H69 (Figure 4C). By contrast, the solvent side of Hsp15 that faces towards the E-site has less positively charged residues and displays in fact a net negative charge (Figure 4D). Within cluster 1 is the highly conserved Arg19 that is located at the distal end of the α1-helix (Figure 1), which approaches the minor groove of the anticodon stem of the P-site tRNA (Figure 4E). Although the resolution precludes visualization of the interaction of Arg19 of Hsp15 with the P-site tRNA, we note that the equivalent Arg11 in RqcP has been reported to form hydrogen bond interaction with the backbone of nucleotide 25 of the P-site tRNA (8–10), thus an analogous interaction is likely for Hsp15. Within cluster 2, arginine residues (Arg10, Arg24 and Arg28) located in helix α1 (Figure 1) and α2 are directed towards the lower region of H69, whereas Ser46 and the conserved Lys44 located within the α2-β1 loop of Hsp15 (Figure 1) come into close proximity with the lower region of H68 (Figure 4F). Arg10 and Arg24 are also highly conserved and the equivalent Arg2 and Arg16 residues in *B. subtilis* RqcP (Figure 1) also establish interactions with the H69 (8–10). Moreover, mutation of Arg16 to Ala in *B. subtilis* RqcP leads to loss of activity due to destabilizing effects of RqcP interaction with the 50S subunit (8). Alignment (based on the 23S rRNA) of the Hsp15-peptidyl-tRNA-50S complex with a 70S ribosome bearing a P-site tRNA (24) reveals that the position of the peptidyl-tRNA in the Hsp15-ribosome complex is shifted compared to the canonical P-site tRNA position (Figure 4G). While the CCA-end and acceptor arm are generally located similarly, with the CCA-end base-paired with the P-loop at the PTC, the anticodon stem has progressively shifted towards the E-site, reaching a maximum displacement of up to 16.5 Å for the nucleotide C32 (Figure 4G). Comparison with the 70S ribosome also reveals that the binding position of Hsp15 on the 50S subunit is incompatible with that on a 70S ribosome due to steric clashes between Arg42 and Glu32 of Hsp15 and nucleotides U697/G785 within h34/h35 of the 16S rRNA, respectively (Figure 4H-I). Together with the shifted position of the P-site tRNA in the presence of Hsp15, these steric

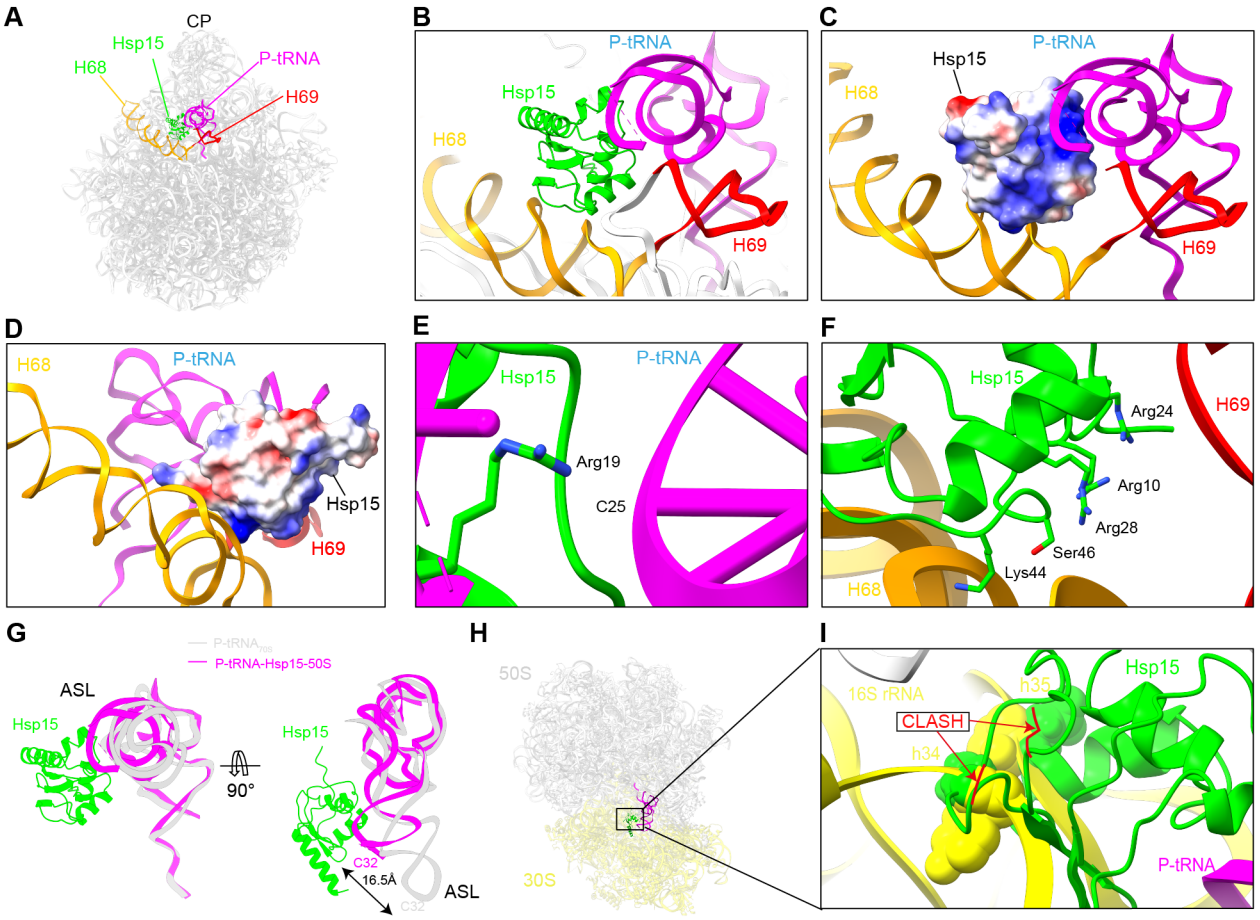

Figure 4. Interactions and structural analysis of *E. coli* Hsp15-peptidyl-tRNA-50S complex. (**A**) Model of *E. coli* Hsp15-peptidyl-tRNA-50S complex highlighting the relative position of Hsp15 (lime) and P-tRNA (magenta) to H68 (orange) and H69 (red) of the 23S rRNA. (**B**) Zoom of (A) showing the localization of Hsp15 (lime) at the base of H68 (orange) and H69 (red) as well as intimate contact with the P-site tRNA (magenta). (**C**) Same view as in (B) but with Hsp15 shown as surface charge distribution where the most positively charged residues form a cluster oriented towards the P-site tRNA, H68 and H69 of the 23S rRNA. (**D**) Solvent side view of Hsp15 showing surface charge distribution with mostly negatively charged residues oriented towards solvent. (**E**) The location of Arg19 in α1 helix of Hsp15 (lime) is located near to nucleotide C25 of the P-site tRNA (magenta). Note that density does not allow a description of interactions. (**F**) Clusters of positively charged residues (Arg10, Arg24, Arg28) within Hsp15 that located in close proximity to H69 (red), whereas Ser46 and Lys44 are in the vicinity of H68 (orange). (**G**) Comparison of P-site tRNA (magenta) from the Hsp15-peptidyl-tRNA 50S complex with canonical P-site tRNA (grey) when bound to a 70S ribosome (PDB ID 7K00) (24). (**H**) Superimposition (based on 23S rRNA alignment) of Hsp15-peptidyl-tRNA-50S complex with a 70S ribosomes (PDB ID 7K00) (24), highlighting in (I) the clashes between Hsp15 (lime) and h34/h35 of 16S rRNA (yellow) of 70S ribosome (PDB ID 7K00) (24).

clashes explain the specificity of Hsp15 for binding to 50S and not 70S ribosomes, as observed here and reported previously (6,7).

A conserved binding site for Hsp15, RqcP and MTRES1 on the 50S subunit

As mentioned, a cryo-EM structure of *E. coli* Hsp15 in complex with a peptidyl-tRNA-50S complex has been determined previously at 10 Å resolution (7). In this study, Hsp15 was reported to bind below the central protuberance where it interacts with H84 of the 23S rRNA and the elbow region of the P-site tRNA (7) (Figure 5A, B). We observe no density for Hsp15 in this region of our complex (Figure 5C) and the reported binding site of Hsp15 is incompatible with our structure and superimposition results in multiple steric clashes with the ribosome as well as the P-site tRNA. In fact, closer inspection reveals that the reported binding site for Hsp15 also produces clashes with the ribosome and P-site tRNA in the previously published model (Supplementary Figure S4A–D), presumably, leading to the generation of three separate PDB entries, namely, for Hsp15 (PDB ID 3BBU), the 50S subunit (PDB ID 3BBX), and the P-site tRNA (PDB ID 3BBV) (7). Even at low threshold, the cryo-EM map density is not sufficient to encompass the molecular model and there is poor correlation between the charge distribution of Hsp15 in the modelled position with interaction surfaces with the rRNA or tRNA (Supplementary Figure S4E, F). Collectively, this leads us to suggest that the low resolution, coupled with a presumably low occupancy of Hsp15 within the complex, led to a mis-assignment of the binding position of Hsp15. Therefore, we favour a model where *E. coli* Hsp15 interacts with the P-site tRNA and H69 (Figure 5E), unlike the previous Hsp15 position (Figure 5F), but instead in an analogous manner to that reported for other S4-domain contain-

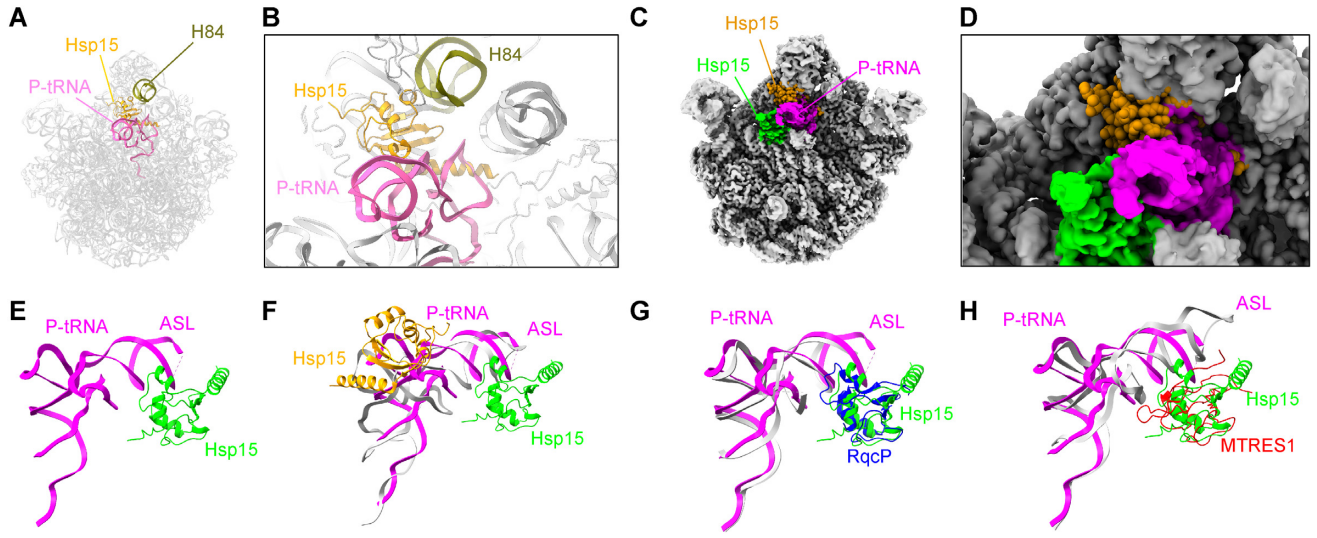

Figure 5. Comparison of Hsp15-peptidyl-tRNA-50S complexes. (**A**) Model of Hsp15-peptidyl-tRNA-50S complex (PDB IDs: 3BBX, 3BBU and 3BBV) from previous study (7), with Hsp15 (orange), P-site tRNA (pink), and H84 of 23S rRNA (olive) highlighted. (**B**) Zoom of (A) showing localization of Hsp15 (orange) between D/T loops of P-site tRNA (pink) and H84 of 23S rRNA (olive). (**C**) Overview and (**D**) Zoom of the superimposition of our cryo-EM density map of Hsp15-peptidyl-tRNA-50S complex (Hsp15, lime; P-site tRNA, magenta, 50S, grey) with model of Hsp15-peptidyl-tRNA-50S complex (Hsp15, orange space-filled representation) from the previous study (7). (**E–H**) Comparison of the relative position of (E) Hsp15 (lime) and P-site tRNA (magenta) from the Hsp15-peptidyl-tRNA-50S complex determined here, with (F) Hsp15 (orange) and P-site tRNA (grey) from previous study (7), (G) RqcP (blue) and P-site tRNA (grey) from B. subtilis RqcP-P-tRNA-50S complex (PDB ID 7AS8) (8–10), and (H) MTRES1 (red) and P-site tRNA (grey) from mitochondrial MTRES1-mtRF-R-P-tRNA-50S complex (PDB ID 7A5H) (13).

ing RNA-binding proteins, such as RqcP (Figure 5G) (8–10) and MTRES1 (Figure 5H) (13). Such a conservation in binding mode is more consistent with the high sequence (Figure 1) and structural homology between these factors (Figure 5E–H).

CONCLUSIONS AND PERSPECTIVE

Together with the available literature (6,7), we present an updated model for the action of Hsp15 during heat shock (Figure 6). Upon heat shock, translating 70S ribosomes and polysomes are converted into 50S-peptidyl-tRNA complexes and the 30S subunits are rapidly degraded (Figure 6A, B). We favour a model where heat shock leads to 70S dissociation, which facilitates rapid 30S degradation (Figure 6A), however, we cannot completely exclude that degradation of the 30S subunit can occur within the context of the 70S ribosomes. Our findings suggest that heat treatment *per se* does not lead to dissociation of 70S ribosomes, raising the possibility that specific splitting factors may be involved dissociating the stressed ribosomes, such as HflX (37–41) or RRF and EF-G (32,42) (Figure 6B). Regardless of how the 50S-peptidyl-tRNA complexes arise, the aberrant nascent chains need to be released from the tRNA so that the 50S subunit and tRNA can be recycled for the next round of translation. Previous structures have suggested that the peptidyl-tRNA on such 50S subunits is flexible and may adopt A- (7) or A/P-site-like (8) states that prevent easy access to the A-site of the peptidyl-transferase center (PTC) on the large subunit (Figure 6B). Here we observe that binding of Hsp15 to peptidyl-tRNA-50S complexes stabilizes the peptidyl-tRNA in a P-site-like state (Figure 6C), where the anticodon stem is shifted even further to the E-site when compared with the relative position on a 70S ribosome (Figure 4G). This state is analogous to that observed previously for RqcP and MTRES1 in complex with peptidyl-tRNA-50S complexes (8–10,13). In *B. subtilis*, RqcP works together with RqcH to add polyalanine tails to the C-terminal end of the aberrant peptidyl-tRNAs (8–11,43), and superimposition of RqcH onto the Hsp15-50S structure suggest that they would be compatible (Supplementary Figure S5A,B). However, since *E. coli* does not have a RqcH homolog, we favour a model where these aberrant peptidyl-tRNAs are simply actively released from the ribosome (Figure 6C). One could imagine that short oligo-peptidyl-tRNAs could simply dissociate from the 50S subunit, analogous to previously reported peptidyl-tRNA drop-off mechanism and would then become the substrate for the peptidyl-tRNA hydrolase (Pth) (43,44). However, our findings that Hsp15 stabilizes the peptidyl-tRNA with the CCA-end inaccessible to Pth at the PTC, suggest that Hsp15 would counteract peptidyl-tRNA drop-off and Pth action, and therefore such complexes would require an additional factor to mediate recycling. Such a factor is unknown in bacteria, however, in mitochondria, MTRES1 was shown to recruit a specialized rescue factor, mtRF-R, to release the aberrant polypeptide chain (13). The N-terminus of mtRF-R has homology with domain III of the canonical release factors RF1 and RF2, and contains the conserved GGQ motif that is critical for mediating peptidyl-tRNA hydrolysis by RFs. Superimposition of mtRF-R onto the Hsp15-50S structures, suggest that Hsp15 binding would be compatible with mtRF-R, and that the C-terminal end of Hsp15 (that is lacking in RqcP) would be in close proximity to interact with mtRF-R or an functional equivalent *E. coli* factor (Supplementary Figure S5C,D). Prime candidates in *E.*

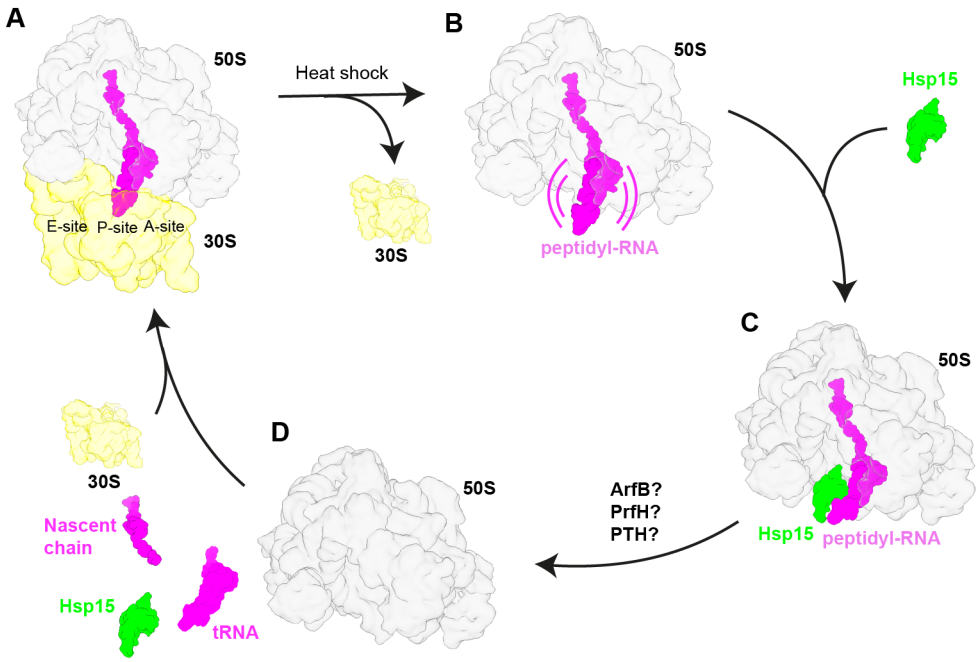

Figure 6. Model for the role of Hsp15 during heat shock. (**A**) Translating 70S ribosomes which undergoes stress in the form of heat shock become unstable and prone to dissociation. (**B**) The prematurely dissociated 50S subunits may still contain peptidyl-tRNA (which is flexible) and is a substrate for the binding of Hsp15. (**C**) Binding of Hsp15 to these peptidyl-tRNA-50S complexes stabilizes the peptidyl-tRNA in a 'P-site'-like state. (**D**) Unknown rescue factors (putative candidates being ArfB, PrfH or PTH) release the nascent chain from the Hsp15-50S-peptidyl tRNA complexes, allowing the free 50S subunits to re-associate with 30S subunits to initiate a new round of translation.

coli for mediating a similar reaction are either the canonical release factors RF1 or RF2, or an RF-related protein, such as the RF homolog PrfH (45,46) or the alternative rescue factor ArfB (43,47), both of which contain a GGQ motifs and are present in *E. coli*. By contrast, we note that in eukaryotes, the aberrant nascent polypeptide chain is released from peptidyl-tRNA-60S complexes by the action of Vms1, which contains a GSQ motif rather than a GGQ (48). Moreover, Vms1-mediated release occurs not via hydrolysis of the peptidyl-tRNA but rather through cleavage of the CCA-end of the tRNA (48–51), therefore, one cannot exclude the possibility that a specialized rescue factor without a GGQ motif may be involved in this process. Identification of the mystery rescue factor for recycling of 50S-peptidyl-tRNA complexes is one of the exciting perspectives for future study in the field.

DATA AVAILABILITY

The cryo-EM map of the Hsp15-peptidyl-tRNA-50S complex and the associated molecular model have been deposited in the Protein Data Bank and Electron Microscopy Data Bank with the accession codes PDB ID: 8AP4 and EMDB ID: 15558 and respectively. Data from tRNA microarray analysis have been deposited in Gene Expression Omnibus (GEO) database with the accession number GSE216100.

SUPPLEMENTARY DATA

Supplementary Data are available at NAR Online.

ACKNOWLEDGEMENTS

We thank Ludo Renault and Willem Noteborn for help with cryo-EM data collection. The electron microscopy data was collected at the Netherlands Center for Electron Microscopy (NeCEN).

FUNDING

Deutsche Forschungsgemeinschaft [WI3285/11-1 to D.N.W.]; Estonian Research Council [PRG335 to T.T.]. Funding for open access charge: University of Hamburg.
Conflict of interest statement. None declared.

REFERENCES

1. Schwarz,E., Lilie,H. and Rudolph,R. (1996) The effect of molecular chaperones on in vivo and in vitro folding processes. *Biol. Chem.*, **377**, 411–416.
2. Richmond,C.S., Glasner,J.D., Mau,R., Jin,H. and Blattner,F.R. (1999) Genome-wide expression profiling in *e. coli* K-12. *Nucleic Acids Res.*, **27**, 3821–3835.
3. Aravind,L. and Koonin,E.V. (1999) Novel predicted RNA-binding domains associated with the translation machinery. *J. Mol. Evol.*, **48**, 291–302.
4. Korber,P., Zander,T., Herschlag,D. and Bardwell,J.C. (1999) A new heat shock protein that binds nucleic acids. *J. Biol. Chem.*, **274**, 249–256.
5. Staker,B.L., Korber,P., Bardwell,J.C. and Saper,M.A. (2000) Structure of hsp15 reveals a novel RNA-binding motif. *EMBO J.*, **19**, 749–757.
6. Korber,P., Stahl,J.M., Nierhaus,K.H. and Bardwell,J.C. (2000) Hsp15: a ribosome-associated heat shock protein. *EMBO J.*, **19**, 741–748.
7. Jiang,L., Schaffitzel,C., Bingel-Erlenmeyer,R., Ban,N., Korber,P., Koning,R.I., de Geus,D.C., Plaisier,J.R. and Abrahams,J.P. (2009)

Recycling of aborted ribosomal 50S subunit-nascent chain-tRNA complexes by the heat shock protein hsp15. *J. Mol. Biol.*, **386**, 1357–1367.
8. Crowe-McAuliffe,C., Takada,H., Murina,V., Polte,C., Kasvandik,S., Tenson,T., Ignatova,Z., Atkinson,G.C., Wilson,D.N. and Hauryliuk,V. (2021) Structural basis for bacterial ribosome-associated quality control by RqcH and rqcP. *Mol. Cell*, **81**, 115–126.
9. Takada,H., Crowe-McAuliffe,C., Polte,C., Sidorova,Z.Y., Murina,V., Atkinson,G.C., Konevega,A.L., Ignatova,Z., Wilson,D.N. and Hauryliuk,V. (2021) RqcH and RqcP catalyze processive poly-alanine synthesis in a reconstituted ribosome-associated quality control system. *Nucleic Acids Res.*, **49**, 8355–8369.
10. Filbeck,S., Cerullo,F., Paternoga,H., Tsaprailis,G., Joazeiro,C.A.P. and Pfeffer,S. (2021) Mimicry of canonical translation elongation underlies alanine tail synthesis in RQC. *Mol. Cell*, **81**, 104–114.
11. Lytvynenko,I., Paternoga,H., Thrun,A., Balke,A., Muller,T.A., Chiang,C.H., Nagler,K., Tsaprailis,G., Anders,S., Bischofs,I. *et al.* (2019) Alanine tails signal proteolysis in bacterial ribosome-associated quality control. *Cell*, **178**, 76–90.
12. Filbeck,S., Cerullo,F., Pfeffer,S. and Joazeiro,C.A.P. (2022) Ribosome-associated quality-control mechanisms from bacteria to humans. *Mol. Cell*, **82**, 1451–1466.
13. Desai,N., Yang,H., Chandrasekaran,V., Kazi,R., Minczuk,M. and Ramakrishnan,V. (2020) Elongational stalling activates mitoribosome-associated quality control. *Science*, **370**, 1105–1110.
14. Gibson,D.G., Young,L., Chuang,R.-Y., Venter,J.C., Hutchison,C.A.,3rd and Smith,H.O. (2009) Enzymatic assembly of DNA molecules up to several hundred kilobases. *Nat. Methods*, **6**, 343–345.
15. Cox,J. and Mann,M. (2008) MaxQuant enables high peptide identification rates, individualized p.p.b.-range mass accuracies and proteome-wide protein quantification. *Nat. Biotechnol.*, **26**, 1367–1372.
16. Schwanhausser,B., Busse,D., Li,N., Dittmar,G., Schuchhardt,J., Wolf,J., Chen,W. and Selbach,M. (2011) Global quantification of mammalian gene expression control. *Nature*, **473**, 337–342.
17. Beckert,B., Turk,M., Czech,A., Berninghausen,O., Beckmann,R., Ignatova,Z., Plitzko,J.M. and Wilson,D.N. (2018) Structure of a hibernating 100S ribosome reveals an inactive conformation of the ribosomal protein s1. *Nat. Microbiol.*, **3**, 1115–1121.
18. Scheres,S.H. (2012) RELION: implementation of a bayesian approach to cryo-EM structure determination. *J. Struct. Biol.*, **180**, 519–530.
19. Kimanius,D., Dong,L., Sharov,G., Nakane,T. and Scheres,S.H.W. (2021) New tools for automated cryo-EM single-particle analysis in RELION-4.0. *Biochem. J.*, **478**, 4169–4185.
20. Zheng,S.Q., Palovcak,E., Armache,J.P., Verba,K.A., Cheng,Y. and Agard,D.A. (2017) MotionCor2: anisotropic correction of beam-induced motion for improved cryo-electron microscopy. *Nat. Methods*, **14**, 331–332.
21. Rohou,A. and Grigorieff,N. (2015) CTFFIND4: fast and accurate defocus estimation from electron micrographs. *J. Struct. Biol.*, **192**, 216–221.
22. Wagner,T., Merino,F., Stabrin,M., Moriya,T., Antoni,C., Apelbaum,A., Hagel,P., Sitsel,O., Raisch,T., Prumbaum,D. *et al.* (2019) SPHIRE-crYOLO is a fast and accurate fully automated particle picker for cryo-EM. *Commun. Biol.*, **2**, 218.
23. Jakobi,A.J., Wilmanns,M. and Sachse,C. (2017) Model-based local density sharpening of cryo-EM maps. *Elife*, **6**, e27131.
24. Watson,Z.L., Ward,F.R., Meheust,R., Ad,O., Schepartz,A., Banfield,J.F. and Cate,J.H. (2020) Structure of the bacterial ribosome at 2 a resolution. *Elife*, **9**, e60482.
25. Goddard,T.D., Huang,C.C., Meng,E.C., Pettersen,E.F., Couch,G.S., Morris,J.H. and Ferrin,T.E. (2018) UCSF chimerax: meeting modern challenges in visualization and analysis. *Protein Sci.*, **27**, 14–25.
26. Pettersen,E.F., Goddard,T.D., Huang,C.C., Meng,E.C., Couch,G.S., Croll,T.I., Morris,J.H. and Ferrin,T.E. (2021) UCSF chimerax: structure visualization for researchers, educators, and developers. *Protein Sci.*, **30**, 70–82.
27. Emsley,P., Lohkamp,B., Scott,W.G. and Cowtan,K. (2010) Features and development of coot. *Acta Crystallogr D Biol. Crystallogr*, **66**, 486–501.
28. Liebschner,D., Afonine,P.V., Baker,M.L., Bunkoczi,G., Chen,V.B., Croll,T.I., Hintze,B., Hung,L.W., Jain,S., McCoy,A.J. *et al.* (2019) Macromolecular structure determination using X-rays, neutrons and electrons: recent developments in phenix. *Acta Crystallogr. D Struct. Biol.*, **75**, 861–877.
29. Chen,V.B., Arendall,W.B. 3rd, Headd,J.J., Keedy,D.A., Immormino,R.M., Kapral,G.J., Murray,L.W., Richardson,J.S. and Richardson,D.C. (2010) MolProbity: all-atom structure validation for macromolecular crystallography. *Acta Crystallogr. D Biol. Crystallogr*, **66**, 12–21.
30. Vila-Sanjurjo,A., Schuwirth,B.S., Hau,C.W. and Cate,J.H.D. (2004) Structural basis for the control of translational initiation during stress. *Nat. Struct. Mol. Biol.*, **11**, 1054–1059.
31. Sharma,M.R., Wilson,D.N., Datta,P.P., Barat,C., Schluenzen,F., Fucini,P. and Agrawal,R.K. (2007) Cryo-EM study of the spinach chloroplast ribosome reveals the structural and functional roles of plastid-specific ribosomal proteins. *Proc. Natl. Acad. Sci. U.S.A.*, **104**, 19315–19320.
32. Sharma,M.R., Donhofer,A., Barat,C., Marquez,V., Datta,P.P., Fucini,P., Wilson,D.N. and Agrawal,R.K. (2010) PSRP1 is not a ribosomal protein, but a ribosome-binding factor that is recycled by the ribosome-recycling factor (RRF) and elongation factor g (EF-G). *J. Biol. Chem.*, **285**, 4006–4014.
33. Polikanov,Y.S., Blaha,G.M. and Steitz,T.A. (2012) How hibernation factors RMF, HPF, and YfiA turn off protein synthesis. *Science*, **336**, 915–918.
34. Woolstenhulme,C.J., Parajuli,S., Healey,D.W., Valverde,D.P., Petersen,E.N., Starosta,A.L., Guydosh,N.R., Johnson,W.E., Wilson,D.N. and Buskirk,A.R. (2013) Nascent peptides that block protein synthesis in bacteria. *Proc. Natl. Acad. Sci. U.S.A.*, **110**, E878–E887.
35. Ude,S., Lassak,J., Starosta,A.L., Kraxenberger,T., Wilson,D.N. and Jung,K. (2013) Translation elongation factor EF-P alleviates ribosome stalling at polyproline stretches. *Science*, **339**, 82–85.
36. Doerfel,L.K., Wohlgemuth,I., Kothe,C., Peske,F., Urlaub,H. and Rodnina,M.V. (2013) EF-P is essential for rapid synthesis of proteins containing consecutive proline residues. *Science*, **339**, 85–88.
37. Zhang,Y., Mandava,C.S., Cao,W., Li,X., Zhang,D., Li,N., Zhang,Y., Zhang,X., Qin,Y., Mi,K. *et al.* (2015) HflX is a ribosome-splitting factor rescuing stalled ribosomes under stress conditions. *Nat. Struct. Mol. Biol.*, **22**, 906–913.
38. Coatham,M.L., Brandon,H.E., Fischer,J.J., Schummer,T. and Wieden,H.-J. (2016) The conserved GTPase HflX is a ribosome splitting factor that binds to the E-site of the bacterial ribosome. *Nucleic Acids Res.*, **44**, 1952–1961.
39. Basu,A. and Yap,M.N. (2017) Disassembly of the staphylococcus aureus hibernating 100S ribosome by an evolutionarily conserved GTPase. *Proc. Natl. Acad. Sci. U.S.A.*, **114**, E8165–E8173.
40. Dey,S., Biswas,C. and Sengupta,J. (2018) The universally conserved GTPase HflX is an RNA helicase that restores heat-damaged escherichia coli ribosomes. *J. Cell Biol.*, **217**, 2519–2529.
41. Srinivasan,K., Dey,S. and Sengupta,J. (2019) Structural modules of the stress-induced protein hflx: an outlook on its evolution and biological role. *Curr. Genet.*, **65**, 363–370.
42. Basu,A., Shields,K.E. and Yap,M.F. (2020) The hibernating 100S complex is a target of ribosome-recycling factor and elongation factor g in staphylococcus aureus. *J. Biol. Chem.*, **295**, 6053–6063.
43. Muller,C., Crowe-McAuliffe,C. and Wilson,D.N. (2021) Ribosome rescue pathways in bacteria. *Front. Microbiol.*, **12**, 652980.
44. Menninger,J.R. (1976) Peptidyl transfer RNA dissociates during protein synthesis from ribosomes of *escherichiacoli*. *J. Biol. Chem.*, **251**, 3392–3398.
45. Maviza,T.P., Zarechenskaia,A.S., Burmistrova,N.R., Tchoub,A.S., Dontsova,O.A., Sergiev,P.V. and Osterman,I.A. (2022) RtcB2-PrfH operon protects *E. coli* ATCC25922 strain from colicin E3 toxin. *Int. J. Mol. Sci.*, **23**, 6453.
46. Tian,Y., Zeng,F., Raybarman,A., Fatma,S., Carruthers,A., Li,Q. and Huang,R.H. (2022) Sequential rescue and repair of stalled and damaged ribosome by bacterial PrfH and rtcB. *Proc. Natl. Acad. Sci. U.S.A.*, **119**, e2202464119.
47. Keiler,K.C. (2015) Mechanisms of ribosome rescue in bacteria. *Nat. Rev. Microbiol.*, **13**, 285–297.
48. Su,T., Izawa,T., Thoms,M., Yamashita,Y., Cheng,J., Berninghausen,O., Hartl,F.U., Inada,T., Neupert,W. and

Beckmann,R. (2019) Structure and function of vms1 and arb1 in RQC and mitochondrial proteome homeostasis. *Nature*, **570**, 538–542.
49. Zurita Rendon,O., Fredrickson,E.K., Howard,C.J., Van Vranken,J., Fogarty,S., Tolley,N.D., Kalia,R., Osuna,B.A., Shen,P.S., Hill,C.P. *et al.* (2018) Vms1p is a release factor for the ribosome-associated quality control complex. *Nat. Commun.*, **9**, 2197.
50. Verma,R., Reichermeier,K.M., Burroughs,A.M., Oania,R.S., Reitsma,J.M., Aravind,L. and Deshaies,R.J. (2018) Vms1 and ANKZF1 peptidyl-tRNA hydrolases release nascent chains from stalled ribosomes. *Nature*, **557**, 446–451.
51. Kuroha,K., Zinoviev,A., Hellen,C.U.T. and Pestova,T.V. (2018) Release of ubiquitinated and Non-ubiquitinated nascent chains from stalled mammalian ribosomal complexes by ANKZF1 and ptrh1. *Mol. Cell*, **72**, 286–302.